Published in final edited form as:
ACS Nano. 2025 January 14; 19(1): 479–487. doi:10.1021/acsnano.4c10039.

Genetically Engineered, Multichromophore Virus-Like Nanoparticles with Ultranarrow Distribution of Emission Intensity

Irina B. Tsvetkova,
Department of Chemistry, Indiana University, Bloomington, Indiana 47405, United States

Nora Roos,
University Hospital Tuebingen, Institute for Medical Virology and Epidemiology of Viral Diseases, Tuebingen 72076, Germany

Lohra M. Miller,
Department of Chemistry, Indiana University, Bloomington, Indiana 47405, United States

Nadia DiNunno,
Department of Microbiology and Immunology, Pennsylvania State University College of Medicine, Hershey, Pennsylvania 17033, United States

Marcel Conrady,
University Hospital Tuebingen, Institute for Medical Virology and Epidemiology of Viral Diseases, Tuebingen 72076, Germany

Domenic Ebert,
University Hospital Tuebingen, Institute for Medical Virology and Epidemiology of Viral Diseases, Tuebingen 72076, Germany

Hauke Lilie,
Institute for Biotechnology and Biochemistry/Technical Biochemistry, Martin-Luther-University Halle-Wittemberg, Halle 06120, Germany

Liam W. Scott,
Department of Chemistry, Indiana University, Bloomington, Indiana 47405, United States

Martin F. Jarrold,
Department of Chemistry, Indiana University, Bloomington, Indiana 47405, United States

Joseph Che-Yen Wang,

Corresponding Author Bogdan Dragnea – dragnea@iu.edu.

ASSOCIATED CONTENT
Supporting Information
The Supporting Information is available free of charge at https://pubs.acs.org/doi/10.1021/acsnano.4c10039.

Thermal stability of GFP-fusion complexes (oligomers and capsids), photophysical properties of sfGFP-VP1 VLPs, structural analysis of cryo-em data, and nanoflow cytometry plots (PDF) Complete contact information is available at: https://pubs.acs.org/10.1021/acsnano.4c10039 The authors declare no competing financial interest.

Department of Microbiology and Immunology, Pennsylvania State University College of Medicine, Hershey, Pennsylvania 17033, United States

Claudia Simon,

University Hospital Tuebingen, Institute for Medical Virology and Epidemiology of Viral Diseases, Tuebingen 72076, Germany; Boehringer Ingelheim Pharma GmbH & Ko. KG, Virus Therapeutics Center, Biberach an der Riss 88397, Germany

Bogdan Dragnea

Department of Chemistry, Indiana University, Bloomington, Indiana 47405, United States

Abstract

Variance in the properties of optical mesoscopic probes is often a limiting factor in applications. In the thermodynamic limit, the smaller the probe, the larger the relative variance. However, specific viral protein cages can assemble efficiently outside the bounds of statistical fluctuations at equilibrium through a process that is characterized by intrinsic quality-control and self-limiting capabilities. In this paper, an approach is described that leverages stoichiometric and structural accuracy in the murine polyoma virus capsid assembly to demonstrate bright, narrowly distributed fluorescence intensity from multichromophore particles that surpass state-of-the-art fluorescent nanosphere probes. Charge-detection mass spectrometry analysis demonstrated that proteins resulting from the fusion of superfolding green fluorescent protein (sfGFP) murine polyoma virus coat proteins self-assemble in vitro into virus-like particles that have similar stoichiometry as virus-like particles formed from wild-type virus coat proteins. Single-particle analysis by total internal reflection fluorescence microscopy provided evidence for a narrow fluorescence intensity that reflects stoichiometric accuracy of the construct.

Graphical Abstract

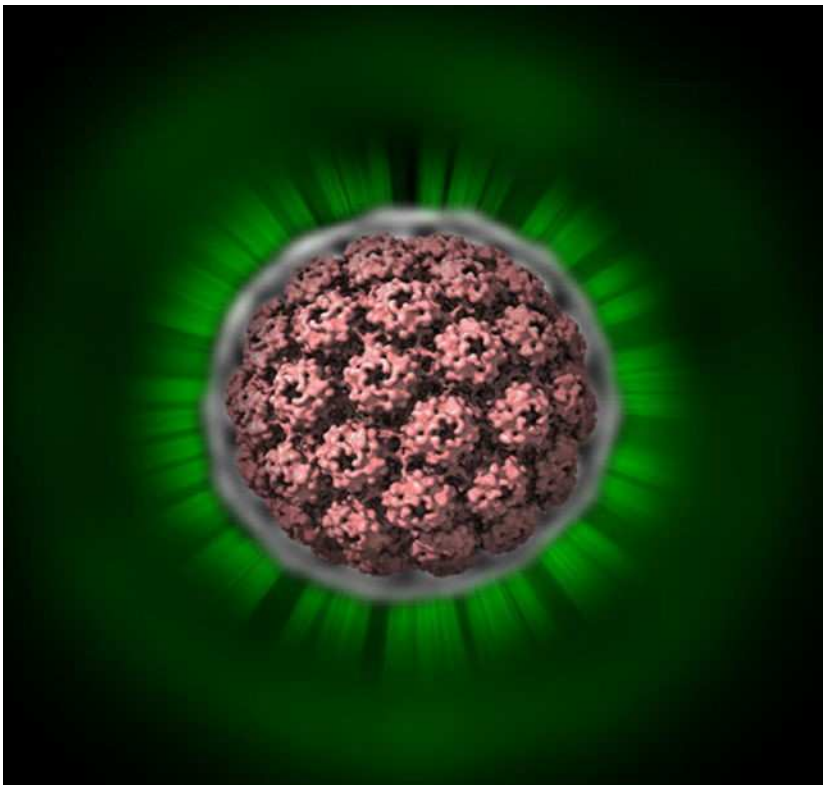

Keywords

murine polyoma virus; virus nanotechnology; nanoflow cytometry; bright fluorescent probes; fluorescent virus-like particles; fluorescent protein fusion

INTRODUCTION

Bioderived nanoparticles are finding myriad applications from cosmetics, to therapeutics and diagnostics.[1,2] Within this class, viruses, phages, and recombinant virus-like particles are seeing an increased presence in biomedical fields including vaccines, targeted carriers for both gene therapy vectors and drugs, and imaging agents.[3–5] Here we describe an in vitro assembled, multichromophore particle derived from the murine polyoma virus (MPyV), which has unique optical properties that make it promising for applications, including but not limited to nanoflow cytometry, in particular.

In fluorescence imaging and sensing applications, employing several chromophores bound to the same targeted functional moiety brings, in principle, the benefit of additive brightness. This is desired, for instance, in conditions of high optical background, like fluorescence image-guided surgery, spectroscopic analysis of multicomponent stock solutions, or, in real-time microscopic imaging applications where both a wide temporal dynamic range and sensitivity are required. In addition, when high spatial resolution is desired, the probe must have dimensions well-below the light wavelength. However, confining multiple fluorescent labels to the volume of a nanoscopic probe comes with limitations. Specifically, when the

distances between nearest-neighbor labels are less than a few nm, efficient homo-Förster resonant energy transfer (FRET) occurs, which increases the number of nonradiative relaxation pathways and decreases the quantum yield and thus, brightness.[6,7]

High-density labeling of nanoscopic probes is thus limited by concentration-induced fluorescence quenching. To provide some quantitative sense, in fluorescence-guided surgery for instance, a tumor-homing antibody is decorated with a few chromophores for visual detection of the tumor during surgical resection.[8,9] However, on a typical antibody with a gyration radius of ~5 nm, no more than two chromophores can be conjugated before concentration quenching of fluorescence to occur.[10]

The issue of brightness at high emitter density is even more critical for the development of near-infrared (NIR) probes for biomedical imaging. Operating within the NIR spectral range allows for deeper tissue penetration. However, attempts at replacing radionuclid labeling by multichromophore NIR fluorescent labeling of sentinel lymph nodes in cancer intraoperative mapping have met with modest success,[11,12] principally due to the weak signals caused by the number of chromophore per label limitation discussed above. Moreover, NIR detectors are generally less sensitive than the ones operating at visible wavelength.

Another application example for multichromophore fluorescence probes used routinely in clinical diagnosis is flow cytometry, where the intensity of fluorescence from labeled monoclonal antibodies is employed as a measure of the antigen expression level. To have a quantitative instrument-independent measure, calibration standards—typically, fluorescentmolecule doped microbeads, are used.

Measuring levels of expression e.g., in sub–100 nm organelles, viruses, or exosomes instead of cells, requires scaling down the calibration standards to nanoscopic sizes. This is currently done simply by employing fluorescent labeled doped nanospheres instead of microbeads.[13] The challenge of extending the use of doped microbead technology to nanoscale is the increase in statistical fluctuations which can become greater than the average itself when the number of labels per nanosphere is reduced to avoid the homo-FRET limitation.

Can we find a way to increase the number of chromophores per probe without affecting the quantum yield by homo-FRET, all the while reducing statistical fluctuations in the number of chromophores per probe? To overcome the double challenge of concentration quenching, as well as of the chromophore number fluctuations from one particle to another that is seen in doped nanospheres, we have explored a route that takes advantage of the innate capability of virus coat proteins to assemble, even in vitro, into cages of near-stoichiometric accuracy, with a narrow mass distribution that sometimes defies expectations from shot-noise statistical fluctuations. This characteristic, encountered in several viruses, was proposed early on to exist due to built-in self-termination and error correction mechanisms in assembly kinetics.[14] Recent theoretical works with experimental backing have identified several nonequilibrium and equilibrium mechanisms.[15–17]

We have designed a fusion protein based on the VP1 capsid protein of the murine polyoma virus (MPyV) which contains the sequence of a green fluorescent protein (GFP) inserted into one of the surface loops of MPyV-VP1. With this construct, we endeavored to exploit

both VP1's capability to assemble efficiently and accurately in vitro, along with an innate resilience of some fluorescent proteins to homo-FRET quenching. The latter is due to the presence of a beta-barrel tightly enclosing the imidazolidin chromophore, which prevents contact in neighboring chromophores. GFPs do not quench by homo-FRET as readily as unprotected chromophores.[18] Further, we have reasoned that, due to the possible steric hindrance of GFPs at the cage surface, spatial fluctuations will be diminished and closepacking favored, with positive consequences for the orientational homogeneity of transition dipoles. These ideas gave us ground to hypothesize that fluorescence quenching should be reduced in GFP-VP1 cages and, if the native icosahedral T = 7 structure that results from normal MPyV VP1 self-assembly[19] were to prevail, we hypothesized that the number of GFPs per particle might be distributed narrowly around the number expected for a T = 7 particle. To test these hypotheses we have employed charge-detection mass spectrometry to identify the mean stoichiometry and variance, cryo-electron microscopy to obtain an average structure of the GFP-VP1 cage, and single-particle spinning disk confocal microscopy to obtain emission intensity statistics from a spread of GFP-VP1 cages, which we compared with those from state-of-the-art dye-doped nanospheres.

RESULTS AND DISCUSSION

MPyV is a nonenveloped, icosahedral, double-stranded DNA virus from the papovaviridae family. The prefix papova- comes from papilloma virus, polyoma virus, and vacuolating agent (SV40), which are representative members of this family.[20] Because papovaviruses are associated with several types of cancer they received considerable interest and have been recently studied in relation to anticancer vaccine development.[21] The MPyV coat consists of three coat proteins: VP1, VP2, and VP3. The coat protein VP1 was shown to spontaneously form virus-like particles (VLPs) when purified from E. coli cells and exposed to appropriate assembly conditions.[22,23] Fully assembled VP1VLPs can be purified from insect[24] or yeast[25] cell systems. Regardless the approach, although some postassembly polymorphism is generally observed, stable VP1VLPs are predominantly formed of 360 molecules of VP1, arranged in 72 pentamers–similar to the architecture of the native virus capsid. As a consequence of structural similarities between VP1VLPs and the native MPyV capsid, essential functional properties are preserved, which make MPyV VLPs interesting for a wide array of nanotechnology/pharmaceutical applications including gene therapy applications.[26]

For GFP fusion we have opted for a superfolding GFP variant (sfGFP) which is known to fold well even when fused to poorly folded polypeptides.[27] Our first goal was to determine whether insertion of a GFP into VP1 will affect the self-assembly of the later.

The mass of the VP1 is 42.5 kDa. The combined mass of the sfGFP and linker is 28 kDa. Because of the size similarity of the VP1 and sfGFP plus linker, to avoid steric clashes at assembly, the fusion sites were chosen on free VP1 loops that are presented on the outside surface of capsid. Previous studies have shown that foreign protein domains can be genetically inserted into the surface-presented HI-loop.[28,29] This methodology allows for the incorporation of exactly one foreign protein domain for every VP1 protein, at equivalent locations in the final assembled MPyV-VLP resulting in 360 GFP proteins incorporated in one VLP.

Molecular models of the constructs are presented in Figure 1. Even when the linker is fully extended, an assembled T = 7 underlying template is expected would impose a dense packing of sfGFPs in the outer layer. In addition, sfGFPs are nominally charged to prevent aggregation.[30] Will steric clashes and electrostatic repulsion prevent self-assembly of the fusion protein? Intriguingly, the answer is “No”.

Self-assembly of sfGFP-VP1VLPs readily occurred when bacteria expressed pentameric sfGFP-VP1 were dialyzed against assembly buffer (see methods for details), which provided a redox shuffiing environment and promoted disulfide bond formation between pentamers.[25] The latter provided enough of a thermodynamic driving force to overcome the steric and electrostatic barriers and stabilize assembly products. The sfGFP-VP1 have similar thermal stability as wtVP1VLPs which confirms that GFP is not significantly affecting protein–protein interactions during VLP asssembly (Figure S1).

Figure 2a shows the result of assembly by negative stain transmission electron microscopy (TEM), after intact VLPs were separated from other species—debris or aggregates—by size exclusion chromatography. The sfGFP layer is easily recognizable, as radially oriented blobs on top of a dense, inner shell. The apparent diameter of round VLPs is ∼62 nm, consistent with expectations from the molecular model, assuming a radially extended linker. By TEM, round particles are the most abundant recognizable entity. Also, there is a population of oval particles, presumably prolate spheroidal in shape, with an average minor axis length of 58.6 ± 5.3 nm and an average major axis length of 64.9 ± 5.9 nm.

The successful assembly of sfGFP-VP1 is evidence that the resultant VP1 fusion proteins retained assembly capabilities despite the relatively large increase in size. All previously reported VP1 fusions had smaller molecular weights relative to sfGFP—before this work largest added protein mass was 19 kDa.[28,29] As sfGFP-VP1 is the largest fusion that has been performed so far that preserves functional capability it points to an unusually strong thermodynamic force driving VP1 assembly.

Spinning disk confocal microscopy of VLPs and fluorescent nanobeads was employed in order to compare VLP fluorescence emission properties with those of an industry standard. Figure 3a shows a typical fluorescence micrograph of sfGFP-VP1VLPs dispersed on a coverslip, in assembly buffer. (Note that the color scale has been chosen to avoid pixel saturation. In other words, the particles look identical because they emit the same amount of light, not because their contrast is saturated, see Methods for imaging details). Figure 3b presents histograms of intensities measured with the EM-CCD detector, from several hundreds of VLPs, and from the same number of 100 nm dye-doped nanobeads.

Table 1 presents the average number of detected photons (for same exposure time) and the root-mean-square-deviation (r.m.s.d) about the mean for VLPs, and for the 100 nm nanobeads. We note that the 100 nm nanobeads emit about three times more photons than the VLPs. However, the volume of the nanobeads is at least 8 times larger than that of VLPs. Emission from VLPs per spherical volume is 2.7× greater than that of nanobeads. Note

that this value represents a lower limit of volume-normalized brightness, since sfGFPs are distributed within a ∼ 4 nm shell, and not within the entire volume of the VLP, like the dyes in nanobeads.

When we consider the actual sfGFP shell volume, the volume-normalized emission is ~10× greater in sfGFP-VP1VLPs than for nanospheres. Also note that, despite the high, effective concentration of sfGFP in the surface shell (above 10 mM), VLPs do not show measurable concentration quenching when fluorescence and fluorescent lifetime of assembled VLPs is compared to free sfGFP-VP1 pentamers or free sfGFP (see Figure S2).

Most importantly, instead of observing statistical fluctuations increasing with decreasing the size of the particle when we examine the r.m.s.d. or the coefficient of variation, we observe the opposite trend: the emission intensity distribution is narrower in VLPs than in nanobeads, although the number of sfGFP chromophores is smaller than the average number of dyes per nanobead. The intriguing departure from expectations based on statistical fluctuations in equilibrium processes is an illustration of "self-control" in virus self-assembly.[14] In other words, when subunits are added to a growing capsid, their conformational state may depend critically on their previous history and what their neighbors are doing, as well as on their own intrinsic interaction properties. Numerical simulations have demonstrated in several cases how such biased, nonequilibrium growth may result in quality (self-)control of assembly.[31,32]

The reduction in the variation coefficient brought by the virus assembly-based approach with respect to randomly doped, similarly sized, state-of-the-art multichromophore probes is encouraging. Nevertheless, from an idealized ensemble of self-assembled particles identical at all scales one would expect intensity fluctuations to be dominated by photon shot-noise (≈0.3%), which is almost 2 orders of magnitude below observed fluctuations. The origins of emission variance in sfGFP-VP1 particles must be different from photon noise. Is the dominant contribution to the variance coming from fluctuations in the number of sfGFPVP1s per particle due to polymorphism at assembly, or does it have a structural origin from spatial and temporal fluctuations in the orientation of transition dipoles on the VLP surface, relative to the VP1 template?

To narrow the possibilities, we have employed charge-detection mass spectrometry (CD-MS). CD-MS is a recently developed single ion measurement technique, which simultaneously measures the mass to charge ratio (m/z) and charge, of individual ions allowing a direct mass measurement of large and heterogeneous analytes. CD-MS has been proven extremely useful in VLP assemblies characterization, previously.[15,33,34] Here, measurements were taken for thousands of sfGFP-VP1VLP ions, enabling the generation of a statistically useful mass histogram for the assembled sfGFP-VP1VLP, Figure 4.

The most probable mass found in CD-MS experiments was 25.1 MDa, which is close to the 25.3 MDa expected from a T = 7 formed of 360 sfGFP-VP1 molecules. The prevalent mass is consistent with a T = 7 structure. The mass r.m.s.d was ~4.9 MD, which corresponds to a variation coefficient of approximately 19.4%. Therefore, the CD-MS-measured mass distribution variance is similar to that found from fluorescence microscopy, which suggests that fluctuations in the number of fluorescent molecules per particle play a role in the origin of particle-to-particle fluctuations in emission. Even so, as we have seen, this variance is much smaller than that obtained from random dye doping of nanospheres.

To address the question of the structure of the sfGFP array at the VLP surface, we have employed cryo-electron microscopy (cryo-EM) with single particle reconstruction. Note that cryo-EM classes do reveal polymorphism increases in sfGFP-VP1VLPs with respect to

VP1VLPs (Figure S3). However, the prevalent structure was consistent with that expected from the model in Figure 1, and with the stoichiometry provided by CD-MS.

The 3D structure of the wtVP1VLP (Figure 5, left) showed the canonical 72 protruding capsomers, with each capsomer composed of 5 VP1 subunits arranged in a T = 7 icosahedral surface lattice.[25] Inside the VLP, we observed a density layer of host RNA (Figure 5, cross section, left). In contrast, the 3D structure of the reassembled sfGFP-VP1VLP (Figure 5, right), which lacked internal RNA, exhibited an additional external density layer at a radius of 28.5 nm. This layer, linked to the top of the VP1 capsomer, is attributed to the sfGFP fusion. The sfGFP layer thickness is about 3.2 nm, less than the expected 6.5 nm for sfGFP plus linker, suggesting an orientation of sfGFP not extending straight from the capsid surface.

Beneath the sfGFP density layer, we observed an intact VP1 capsid shell. Like the wtVP1VLP, the sfGFP-VP1VLP clearly showed a symmetric arrangement of subunits and consisted of 72 protruding capsomers (Figure 5, cross section, right). The 2D radial density profile (Figure S5) showed that the capsomer organization in the sfGFP-VP1VLP was virtually identical to that of the wtVP1VLP (top two rows in Figure S5), with the exception of a slightly weaker density at the bottom of the pentameric capsomer in the sfGFP-VP1VLP. This slight difference, possibly due to the absence of nucleic acids, did not compromise the integrity of the VLPs.

However, due to the icosahedral averaging in the data processing, the sfGFP density appeared fused and was shorter than a typical 5 nm of sfGFP. To better understand the sfGFP organization and orientation on the VP1 shell, we conducted asymmetric 3D reconstruction (Figure S4). The asymmetric 3D structure, albeit at lower resolution, showed the same VP1 capsomer organization as the symmetrized structure (Figure S5, third row). The sfGFP density was composed of several short cylinder segments, resembling the shape of sfGFP. Fitting the atomic model of GFP into the cryo-EM density revealed variations in the orientation and position of sfGFPs across the capsid, with only partial local order around the 5-fold axes of the VP1 shell (Figure S4). Thus, the prevalent structure obtained from cryo-EM is consistent with the most probable stoichiometry inferred from CD-MS experiments.

The partially disordered sfGFP layer suggests the presence of spatial fluctuations in the chromophore transition dipole orientation. Coupling with the excitation field will reflect this heterogeneity and contribute to the intensity variance. Thus, it appears that both fluctuations in stoichiometry and in the molecular orientations of sfGFP are responsible for the observed 21% variance in intensity, with stoichiometric variance being the dominant factor.

So far, our findings indicate that the structural VP1 proteins of MPyV can assemble vigorously enough to overcome steric constraints from fluorescent proteins fusions on the outside of the capsid. We note that internal loops facing the lumenal cavity are also available, which raises the possibility of decorating the shell with two concentric layers of chromophores of two different colors, although we have not followed this possibility here.[35] Brillault et al. reported previously of a blue tongue virus based concentric arrangement of chromophores, with the outer layer being formed of 120 GFPs genetically fused, while the inner was formed by a fluorescent bioconjugate, stochastically bound.[36]

Such arrangements of symmetric chromophores situated at a few nm proximity from each other form a coupled emitter network and may offer tantalizing examples of cooperative photonic properties. For instance, similar multichromophore virus-like particles were recently discovered to exhibit superradiant emission at room temperature, in liquid.[37–39]

Finally, to illustrate the potential level of performance for nanoflow cytometry applications, we compared sfGFP-VP1VLPs with fluorescent 100 nm nanobeads on a commercial instrument. Commonly, for samples above 200 nm diameter the scattering signal is used as trigger to start the measurement. However, biological samples, particularly thin layer shells like VLPs or liposomes, with dimensions below 200 nm have much less scattering than solid nanobeads used as standards. Thus, for our measurements triggering was done on the fluorescence channel B488–525 While sfGFP-VP1VLPs cannot be discriminated from background in the scattering channel (with a 405 nm laser), fluorescence is easily detected and provides a narrow signal compared to the 100 nm beads control (Figure S6). The emission intensity distribution measured by nanoflow cytometry was similar to that obtained from single particle confocal microscopy.

CONCLUSION

In summary, we report the possibility of adding bright fluorescence emission to in vitro self-assembled MPyV VP1 by fusing sfGFP and VP1. Despite its size, the addition of sfGFP via a sufficiently flexible linker does not hinder appreciably the self-assembly properties of VP1. CD-MS was employed to determine VLPs stoichiometry, and cryo-EM for their structure. The latter suggested that the VP1 is arranged on a T = 7 icosahedral shell formed of 72 pentameric oligomers, surrounded by a partially ordered shell of ~60 nm diameter formed of 360 sfGFPs. These bioderived particles are brighter per unit volume than commercial, state-of-the-art 100 nm dye-doped nanobeads, and have a much narrower intensity distribution, which potentially makes them useful as standards in nanoflow cytometry for the measurement of protein expression in subcellular biological nanoparticles.

Looking forward, it is worthwhile noting that, while we have yet to explore conditions of assembly and separation that would possibly lead to a narrower stoichiometry and a more homogeneous population overall, in the future, such an endeavor, combined with insights from molecular dynamics simulations could lead to a more relaxed, closer packed sfGFP layer with longer-range rotational symmetry and thus, to further narrowing of the intensity distribution. Whether these future improvements will come to pass or not, the sfGFPVP1VLP approach has already led to the narrowest fluorescence intensity distribution to date for a particle of tens of nm in size.

EXPERIMENTAL SECTION

Plasmid Construction.

The gene of sfGFP was first cloned into pETSUMOadapt as described previously.[40] Then, the gene encoding sfGFP (from pETSUMOadapt-sfGFP) was cloned into the VP1 gene (Mouse Polyomavirus small plaque strain 16) in the pALtac-VP1 plasmid[23] via Gibson cloning at the HI-loop after amino acid position N294 with N-terminal GSGSSH and C-terminal GSSGSGS linker (Figure 6).

Protein Expression, Purification and VLP Assembly.

The plasmids pALtac-sfGFP-VP1 or pETSUMOadapt-sfGFP were transformed in BL21 or BL21(DE3), respectively, and selected on LB-Ampicillin or LB-Kanamycin plates, respectively. The preculture 200 mL LB-Medium/Kanamycin or Ampicillin were inoculated with a single colony and grown overnight at 37 °C. Four L of TB-medium/Kanamycin or Ampicillin (1 L medium in 5 L baffled shaking flasks) were inoculated with the preculture to an OD600 of 0.2 and incubated at 37 °C (sfGFP) or 16 °C (sfGFP-VP1) at 100 rpm. At an OD600 of 1 expression was induced by the addition of 1 mM IPTG and cells were harvested at an OD600 of 5 (30 g/L wet biomass) by centrifugation at 8 000 g, 8 °C, 15 min. Cell pellets were stored at −20°C.

sfGFP: 13 g of wet biomass were resuspended in 30 mL 50 mM Tris·HCl pH 8 at 8 °C, 200 mM NaCl, 5% Glycerol), 3 mM MgCl_2, 7 μL Benzonase (Merck, purity grade II), protease inhibitor cocktail (Roche, cOmplete EDTA free), 3.5 mg/mL Lysozym (Carl Roth) and incubated 30 min at 8 °C while stirring. Cells were lysed by 3 cycles at 1000 psi using the FRENCH press (Thermo electron). Lysate was clearified by centrifugation at 20 000 g, 30 min, 8 °C. The supernatant was applied to Ni-NTA (Histrap fast flow 5 mL). The His6-SUMO-sfGFP fusion was cleaved by His6-SUMO-Protease[41] at 1:1 w/w 16 h at 8 °C, concomitantly dialyzed against 50 mM Tris· HCl pH 8 at 8 °C, 5% (v/v) glycerol, 200 mM NaCl and applied to Ni-NTA again. The flow through, containing sfGFP, was applied to size exclusion chromatography (Superdex S75 XK16/60, GE healthcare). Fractions were pooled, frozen in liquid nitrogen and stored at −25 °C. The final yield of monomeric sfGFP was 80 mg with >95% purity. sfGFP-VP1: In analogy to the VP1-pentamer production as described in Burkert et al.,[42] sfGFP-VP1 was produced in bacterial cells as pentameric subunits. ~20 g of wet biomass were resuspended in 30 mL 200 mM Tris·HCl pH 8 at 8 °C, 200 mM NaCl, 5% Glycerol, 10 mM DTT, 3 mM $MgCl_2$, 7 μL Benzonase (Merck, purity grade II), protease inhibitor cocktail (Roche, cOmplete EDTA free), 3.5 mg/mL lysozyme (Carl Roth) and incubated 30 min at 8 °C while stirring. Cells were lysed by 3 cycles at 1000 psi using the FRENCH press (Thermo electron). Lysate was diluted 1:10 in 50 mM Tris·HCl pH 8 at 8 °C, 200 mM NaCl, 5% Glycerol, 0.5 mM TCEP, 3 mM $MgCl_2$ and incubated one hour at 8 °C. Benzonase reaction was stopped by the addition of 10 mM EDTA. Protamine sulfate (5% w/v in MQ-H2O) was added dropwise to the lysate until 0.5% w/v protamine sulfate was reached. The lysate was clarified by centrifugation at 30 000 g, 30 min, 8 °C. The clear, green supernatant was adjusted to 2 M ammonium sulfate by adding solid pestled powder while stirring and incubated 30 min at 8 °C. The precipitated sfGFP-VP1 was resuspended in 40 mL 50 mM Tris·HCl pH 8 at 8 °C, 200 mM NaCl, 5% glycerol, 0.5 mM TCEP, 5 mM EDTA, 50 mM DTT and dialyzed against 50 mM Tris·HCl pH 8 at 8 °C, 200 mM NaCl, 5% Glycerol, 0.5 mM TCEP, 5 mM EDTA overnight followed by centrifugation for 30 min, 16 000 g, 8 °C and filtration (0.45 μm). Filtrate was applied to size exclusion chromatography (Superdex S200 XK16/60, GE healthcare) equilibrated with 50 mM Tishk pH 7.4 at 8°C, 200 mM NaCl, 5% Glycerol, 0.5 mM TCEP, 5 mM EDTA. Pentamer fractions of (V_E 55–65 mL) were pooled and concentrated to 1 mg/mL of sfGFP-VP1 and assembled by dialysis against assembly buffer (50 mM Tris·HCl pH 7.4 at 22 °C, 200 mM NaCl, 5% Glycerol, 0.4 M $(NH_4)_2SO_4$, 0.5 mM GSH, 4.5 mM GSSG) 48 h at 22 °C. Samples were centrifuged at 20 000 g, 30 min, 20 °C and loaded on a Superdex S500 XK26/60 (GE healthcare) equilibrated with 50 mM Tris·HCl pH 7.4 at 8 °C, 5% (v/v) glycerol, 200 mM NaCl. Elution volumes of ~148 mL correspond to sfGFP-VP1-VLPs, fractions were pooled, frozen in liquid nitrogen and stored at −25 °C. This protocol yielded ~30 mg of purified sfGFPVP1-VLPs.

Scanning Disk Confocal Microscopy.

Single particle fluorescence imaging was performed on a Dragonfly 505 microscope system (Andor Technology, South Windsor, CT) with an inverted Nikon Ti2 microscope and confocal scanning unit. Samples were excited and imaged through a high-power oilimmersion objective (CFI APO TIRF, NA 1.49, 100× Nikon). Excitation laser wavelength was 488 nm. Fluorescence was collected by the same objective, passed through an emission filter 521/38 and recorded by an iXon Life 888 EMCCD Camera with 50 ms exposure time (Andor Technology, Inc.). Images were processed and analyzed using Andor Solis, ImageJ and IgorPro software.

Negatively Stained Electron Microscopy.

Electron-transparent samples were prepared by placing 10 μL of dilute (≈0.01 mg/mL) sample onto a carbon-coated copper grid. After 10 min, the excess solution on the grid was removed with filter paper. Grid was stained with 10 μL of 2% uranyl acetate for 10 min and the excess solution was removed by blotting with filter paper. The sample was then left to dry for several minutes. Images were acquired at an accelerating voltage of 80 kV on a JEOL JEM 1010 Transmission electron microscope and analyzed with the ImageJ Processing Toolkit.

Steady State Absorption and Fluorescence Emission Spectroscopy.

UV–visible absorbance spectra were collected using a Varian Cary 100 Bio instrument. Fluorescence measurements were conducted on QuantaMaster fluorescence spectrometer (Horiba) with the following parameters: excitation wavelength: 488 nm; emission wavelength: 515 nm. The excitation and steady-state emission spectra of solutions at the same OD_488 were an average of at least three independent measurements.

Charge-Detection Mass Spectrometry.

CD-MS measurements were performed on a home-built prototype instrument described in detail elsewhere.[43,44] Briefly, ions were generated via a commercial nanoelectrospray source (TriVersa Nanomate, Advion, Ithaca, NY) and entered the instrument through a metal capillary. Subsequently, ions were thermalized and desolvated within a FUNPET interface.[45] Following this, ions pass through a series of ion optics and are focused into a dual hemispherical deflection energy analyzer for energy filtration, isolating a narrow band of kinetic energies centered on 100 eV/z. The ions are then focused into an electrostatic linear ion trap (ELIT) where a conduction cylinder is housed.[46] Trapped ions oscillate back and forth through the conduction cylinder and the induced charge is detected by a charge sensitive amplifier. The resulting signal is digitized and analyzed using fast Fourier transforms (FFTs) such that the oscillation frequency yields the m/z and the FFT magnitude is proportional to the charge. Ions are trapped for 100 ms. Prior to ion introduction, sfGFPVP1VLPs were transferred into a volatile salt solution (200 mM ammonium acetate, 2 μM calcium acetate) using Zeba micro spin columns (Thermo Scientific, 89877).

Cryo-EM.

To prepare cryo-EM specimen, 4 μL of sample solution was applied on a glow-discharged continuous carbon film coated copper grid (EMS). The grid was frozen using an FEI Vitrobot (Mark III and Mark IV)with the following settings: 25 s wait time, 4 s blotting time, and 100% humidity in Mark III or 15 s blotting time, 0 blotting force, and 100%

humidity in Mark IV. Frozen hydrated cryo-EM grids were then transferred 300 kV Titan Krios G3i or 200 kV Talos Arctica (Thermo Fisher Scientific). Data collection was done with EPU automation software under low dose setup where images were acquired on a Gatan K3 or a TFS Falcon III direct electron detector in electron counting mode. For each image, a total dose of 30 e-/Å^2 was used with frame dose rate at 1 e-/Å^2. The effective pixel size for both data was 0.84 Å. Particle picking was done semimanually using e2boxer.py in EMAN2 (v2.23).[47] Motion correction, 2D classification, initial model building, and 3D refinement were performed using Relion (v3.0.8).[48] Focus refinement was performed using the protocol established earlier.[49,50] The 3D structures were visualized using UCSF Chimera[51] and ChimeraX.[52]

Nano-Flow Cytometry.

Nanoflow cytometry was performed using a CytoFLEX system (Beckman Coulter, Pasadena, CA) equipped with four lasers (405, 488, 561, and 640 nm wavelength). The 488 nm laser channel was used for trigger option with manual threshold setting of 2500 and gain 3000 in the acquisition setting. Samples were loaded and run with a slow flow rate (10 μL/min) for 5 min until the event/s rate became stable, and then 1 min acquisition run was saved. Data were acquired and analyzed using CytExpert software (Beckman Coulter).

Supplementary Material

Refer to Web version on PubMed Central for supplementary material.

ACKNOWLEDGMENTS

This work was possible due to support from the U.S. Army Research Office, Extreme Materials Branch, through award # W911NF2010072 to B.D., from the National Science Foundation through award # 2232717 to B.D., from NIH grant R21-AI1641191 and R01AI173104 to J.C.-Y.W. We thank The Pennsylvania State University College of Medicine for access to Cryo-EM (RRID: SCR_021178) and the HPC core facilities. We are grateful to the Center for Bioanalytical Metrology (CBM), an NSF Industry-University Cooperative Research Center, for providing funding for this project under grant NSF IIP 1916645, and to members of the industry advisory board of the CBM for valuable discussions and feedback, specifically to Christopher Welch, Ph.D from Indiana Consortium for Analytical Science and Engineering and Michael W. Olszowy, Ph.D from Sartorius. We are also grateful to Sarah Cox-Vazquez, Ph.D. and the IUB Flow Cytometry Core Facility for access to the CytoFLEX LX instrument - this equipment was funded in part by the IU Office of Research through the Research Equipment Fund.

ABBREVIATIONS

MPyV	murine polyoma virus
TEM	transmission electron microscopy
CD-MS	charge-detection mass spectrometry

REFERENCES

(1). Wen AM; Steinmetz NF Design of virus-based nanomaterials for medicine, biotechnology, and energy. Chem. Soc. Rev. 2016, 45, 4074–4126. [PubMed: 27152673]

(2). Yip LX; Wang J; Xue Y; Xing K; Sevencan C; Ariga K; Leong DT Cell-derived nanomaterials for biomedical applications. Sci. Technol. Adv. Mater. 2024, 25, 2315013. [PubMed: 38476511]

(3). Benjamin C; Brohlin O; Shahrivarkevishahi A; Gassensmith JJ Micro and Nano Technologies. In Nanoparticles for Biomedical Applications, Chung EJ; Leon L; Rinaldi C, Eds.; Elsevier, 2020, pp. 153–174.

(4). Comas-Garcia M; Colunga-Saucedo M; Rosales-Mendoza S. The Role of Virus-Like Particles in Medical Biotechnology. Mol. Pharmaceutics 2020, 17, 4407–4420.

(5). Pumpens P; Pushko P. Virus-Like Particles A Comprehensive Guide; CRC Press, 2024.

(6). Valeur B; Berberan-Santos MN Molecular Fluorescence: Principles and Applications, 2nd ed.; John Wiley & Sons, 2013.

(7). Reineck P; Francis A; Orth A; Lau DWM; Nixon-Luke RDV; Rastogi ID; Razali WAW; Cordina NM; Parker LM; Sreenivasan VKA; Brown LJ; Gibson BC Brightness and Photostability of Emerging Red and Near-IR Fluorescent Nanomaterials for Bioimaging. Adv. Opt. Mater. 2016, 4, 1549–1557.

(8). Zhang RR; Schroeder AB; Grudzinski JJ; Rosenthal EL; Warram JM; Pinchuk AN; Eliceiri KW; Kuo JS; Weichert JP Beyond the margins: Real-time detection of cancer using targeted fluorophores. Nat. Rev. Clin. Oncol. 2017, 14, 347–364. [PubMed: 28094261]

(9). Tipirneni KE; Warram JM; Moore LS; Prince AC; de Boer E; Jani AH; Wapnir IL; Liao JC; Bouvet M; Behnke NK; Hawn MT; Poultsides GA; Vahrmeijer AL; Carroll WR; Zinn KR; Rosenthal E. Oncologic Procedures Amenable to Fluorescence-guided Surgery. Ann. Surg. 2017, 266, 36–47. [PubMed: 28045715]

(10). Haugland RP Coupling of monoclonal antibodies with fluorophores. In Monoclonal Antibody Protocols, Davis WC, Ed.; Humana Press, 1995, Vol. 45, pp 205–221. DOI:.

(11). Verbeek FP; Troyan SL; Mieog JSD; Liefers GJ; Moffitt LA; Rosenberg M; Hirshfield-Bartek J; Gioux S; Van De Velde CJ; Vahrmeijer AL; Frangioni JV Near-infrared fluorescence sentinel lymph node mapping in breast cancer: A multicenter experience. Breast Cancer Res. Treat. 2014, 143, 333–342. [PubMed: 24337507]

(12). Stoffels I; Dissemond J; Pöppel T; Schadendorf D; Klode J. Intraoperative fluorescence imaging for sentinel lymph node detection: Prospective clinical trial to compare the usefulness of indocyanine green vs technetium Tc 99m for identification of sentinel lymph nodes. JAMA Surg. 2015, 150, 617–623. [PubMed: 26017057]

(13). Lian H; He S; Chen C; Yan X. Flow Cytometric Analysis of Nanoscale Biological Particles and Organelles. Annu. Rev. Anal. Chem. 2019, 12, 389–409.

(14). Caspar D. Self-control of self-assembly. Curr. Biol. 1991, 1, 30–32. [PubMed: 15336200]

(15). Lutomski CA; Lyktey NA; Zhao Z; Pierson EE; Zlotnick A; Jarrold MF Hepatitis B Virus Capsid Completion Occurs through Error Correction. J. Am. Chem. Soc. 2017, 139, 16932–16938. [PubMed: 29125756]

(16). Panahandeh S; Li S; Marichal L; Leite Rubim R; Tresset G; Zandi R. How a Virus Circumvents Energy Barriers to Form Symmetric Shells. ACS Nano 2020, 14, 3170–3180. [PubMed: 32115940]

(17). Hagan MF; Grason GM Equilibrium mechanisms of self-limiting assembly. Rev. Mod. Phys. 2021, 93, 025008. [PubMed: 35221384]

(18). Chudakov DM; Matz MV; Lukyanov S; Lukyanov KA Fluorescent proteins and their applications in imaging living cells and tissues. Physiol. Rev. 2010, 90, 1103–1163. [PubMed: 20664080]

(19). Stehle T; Harrison SC Crystal structures of murine polyomavirus in complex with straightchain and branched-chain sialyloligosaccharide receptor fragments. Structure 1996, 4, 183–194. [PubMed: 8805524]

(20). Pfister H. Laboratory Diagnosis of Infectious Diseases Principles and Practice: Volume II Viral, Rickettsial, and Chlamydial Diseases; Springer New York: New York, NY, 1988; pp. 301–316.

(21). Signorelli C; Odone A; Ciorba V; Cella P; Audisio RA; Lombardi A; Mariani L; Mennini FS; Pecorelli S; Rezza G; Zuccotti GV; Peracino A. Human papillomavirus 9-valent vaccine for cancer prevention: A systematic review of the available evidence. Epidemiol. Infect. 2017, 145, 1962–1982. [PubMed: 28446260]

(22). Salunke DM; Caspar DL; Garcea RL Self-assembly of purified polyomavirus capsid protein VP1. Cell 1986, 46, 895–904. [PubMed: 3019556]

(23). Leavitt AD; Roberts TM; Garcea RL Polyoma virus major capsid protein, VP1. Purification after high level expression in Escherichia coli. J. Biol. Chem. 1985, 260, 12803–12809. [PubMed: 2995391]

(24). Montross L; Watkins S; Moreland R; Mamon H; Caspar D; Garcea R. Nuclear assembly of polyomavirus capsids in insect cells expressing the major capsid protein VP1. J. Virol. 1991, 65, 4991–4998. [PubMed: 1651418]

(25). Simon C; Klose T; Herbst S; Han BG; Sinz A; Glaeser RM; Stubbs MT; Lilie H. Disulfide linkage and structure of highly stable yeastderived virus-like particles of murine polyomavirus. J. Biol. Chem. 2014, 289, 10411–10418. [PubMed: 24567335]

(26). Forstová J; Krauzewicz N; Sandig V; Elliott J; Palková Z; Strauss M; Griffin BE Polyoma virus pseudocapsids as efficient carriers of heterologous DNA into mammalian cells. Hum. Gene Ther. 1995, 6, 297–306. [PubMed: 7779913]

(27). Pédelacq J-D; Cabantous S; Tran T; Terwilliger TC; Waldo GS Engineering and characterization of a superfolder green fluorescent protein. Nat. Biotechnol. 2006, 24, 79–88. [PubMed: 16369541]

(28). Gleiter S; Stubenrauch K; Lilie H. Changing the surface of a virus shell fusion of an enzyme to polyoma VP1. Protein Sci. 1999, 8, 2562–2569. [PubMed: 10631971]

(29). Pattinson DJ; Apte SH; Wibowo N; Chuan YP; Rivera-Hernandez T; Groves PL; Lua LH; Middelberg APJ; Doolan DL Chimeric Murine Polyomavirus Virus-Like Particles Induce Plasmodium Antigen-Specific CD8(+) T Cell and Antibody Responses. Front. Cell. Infect. Microbiol. 2019, 9, 215. [PubMed: 31275867]

(30). Laber JR; Dear BJ; Martins ML; Jackson DE; DiVenere A; Gollihar JD; Ellington AD; Truskett TM; Johnston KP; Maynard JA Charge Shielding Prevents Aggregation of Supercharged GFP Variants at High Protein Concentration. Mol. Pharmaceutics 2017, 14, 3269–3280.

(31). Panahandeh S; Li S; Dragnea B; Zandi R. Virus Assembly Pathways Inside a Host Cell. ACS Nano 2022, 16, 317–327. [PubMed: 35019271]

(32). Videbaek TE; Fang H; Hayakawa D; Tyukodi B; Hagan MF; Rogers WB Tiling a tubule: How increasing complexity improves the yield of self-limited assembly. J. Phys.: Condens. Matter 2022, 34, 134003.

(33). Bond K; Tsvetkova IB; Wang JC-Y; Jarrold MF; Dragnea B. Virus Assembly Pathways: Straying Away but Not Too Far. Small 2020, 16, 2004475.

(34). Bond KM; Lyktey NA; Tsvetkova IB; Dragnea B; Jarrold MF Disassembly Intermediates of the Brome Mosaic Virus Identified by Charge Detection Mass Spectrometry. J. Phys. Chem. B 2020, 124, 2124–2131. [PubMed: 32141748]

(35). Dashti NH; Abidin RS; Sainsbury F. Programmable In Vitro Coencapsidation of Guest Proteins for Intracellular Delivery by Virus-like Particles. ACS Nano 2018, 12, 4615–4623. [PubMed: 29697964]

(36). Brillault L; Jutras PV; Dashti N; Thuenemann EC; Morgan G; Lomonossoff GP; Landsberg MJ; Sainsbury F. Engineering Recombinant Virus-like Nanoparticles from Plants for Cellular Delivery. ACS Nano 2017, 11, 3476–3484. [PubMed: 28198180]

(37). Tsvetkova IB; Anil Sushma A; Wang JCY; Schaich WL; Dragnea B. Radiation Brightening from Virus-like Particles. ACS Nano 2019, 13, 11401–11408. [PubMed: 31335115]

(38). Anil Sushma A; Zhao B; Tsvetkova IB; Pérez-Segura C; Hadden-Perilla JA; Reilly JP; Dragnea B. Subset of Fluorophores Is Responsible for Radiation Brightening in Viromimetic Particles. J. Phys. Chem. B 2021, 125, 10494–10505. [PubMed: 34507491]

(39). Holmes J; Sushma AA; Tsvetkova IB; Schaich WL; Schaller RD; Dragnea B. Ultrafast Collective Excited-State Dynamics of a Virus-Supported Fluorophore Antenna. J. Phys. Chem. Lett. 2022, 13, 3237–3243.

(40). Bosse-Doenecke E; Weininger U; Gopalswamy M; Balbach J; Knudsen SM; Rudolph R. High yield production of recombinant native and modified peptides exemplified by ligands for Gprotein coupled receptors. Protein Expression Purif. 2008, 58, 114–121.

(41). Mossessova E; Lima CD Ulp1-SUMO Crystal Structure and Genetic Analysis Reveal Conserved Interactions and a Regulatory Element Essential for Cell Growth in Yeast. Mol. Cell 2000, 5, 865–876. [PubMed: 10882122]

(42). Burkert O; Kreβner S; Sinn L; Giese S; Simon C; Lilie H. Biophysical characterization of polyomavirus minor capsid proteins. Biol. Chem. 2014, 395, 871–880. [PubMed: 24713574]

(43). Contino NC; Jarrold MF Charge detection mass spectrometry for single ions with a limit of detection of 30 charges. Int. J. Mass Spectrom. 2013, 345–347, 153–159. A special Issue honoring Keith R. Jennings and James H. Scrivens.

(44). Contino NC; Pierson EE; Keifer DZ; Jarrold MF Charge Detection Mass Spectrometry with Resolved Charge States. J. Am. Soc. Mass Spectrom. 2013, 24, 101–108. [PubMed: 23197308]

(45). Draper BE; Anthony SN; Jarrold MF The FUNPET—a New Hybrid Ion Funnel-Ion Carpet Atmospheric Pressure Interface for the Simultaneous Transmission of a Broad Mass Range. J. Am. Soc. Mass Spectrom. 2018, 29, 2160–2172. [PubMed: 30112619]

(46). Schmidt HT; Cederquist H; Jensen J; Fardi A. Conetrap: A compact electrostatic ion trap. Nucl. Instrum. Methods Phys. Res., Sect. B 2001, 173, 523–527.

(47). Ludtke SJ Single-Particle Refinement and Variability Analysis in EMAN2.1. Methods Enzymol. 2016, 579, 159–189. [PubMed: 27572727]

(48). Scheres SH Processing of Structurally Heterogeneous Cryo-EM Data in RELION. Methods Enzymol. 2016, 579, 125–157. [PubMed: 27572726]

(49). Ilca SL; Kotecha A; Sun X; Poranen MM; Stuart DI; Huiskonen JT Localized reconstruction of subunits from electron cryomicroscopy images of macromolecular complexes. Nat. Commun. 2015, 6, 8843. [PubMed: 26534841]

(50). Schlicksup CJ; Laughlin P; Dunkelbarger S; Wang JC-Y; Zlotnick A. Local Stabilization of Subunit–Subunit Contacts Causes Global Destabilization of Hepatitis B Virus Capsids. ACS Chem. Biol. 2020, 15, 1708–1717. [PubMed: 32369333]

(51). Pettersen EF; Goddard TD; Huang CC; Couch GS; Greenblatt DM; Meng EC; Ferrin TE UCSF Chimera–a visualization system for exploratory research and analysis. J. Comput. Chem. 2004, 25, 1605–1612. [PubMed: 15264254]

(52). Goddard TD; Huang CC; Meng EC; Pettersen EF; Couch GS; Morris JH; Ferrin TE UCSF ChimeraX: Meeting modern challenges in visualization and analysis. Protein Sci. 2018, 27, 14–25. [PubMed: 28710774]

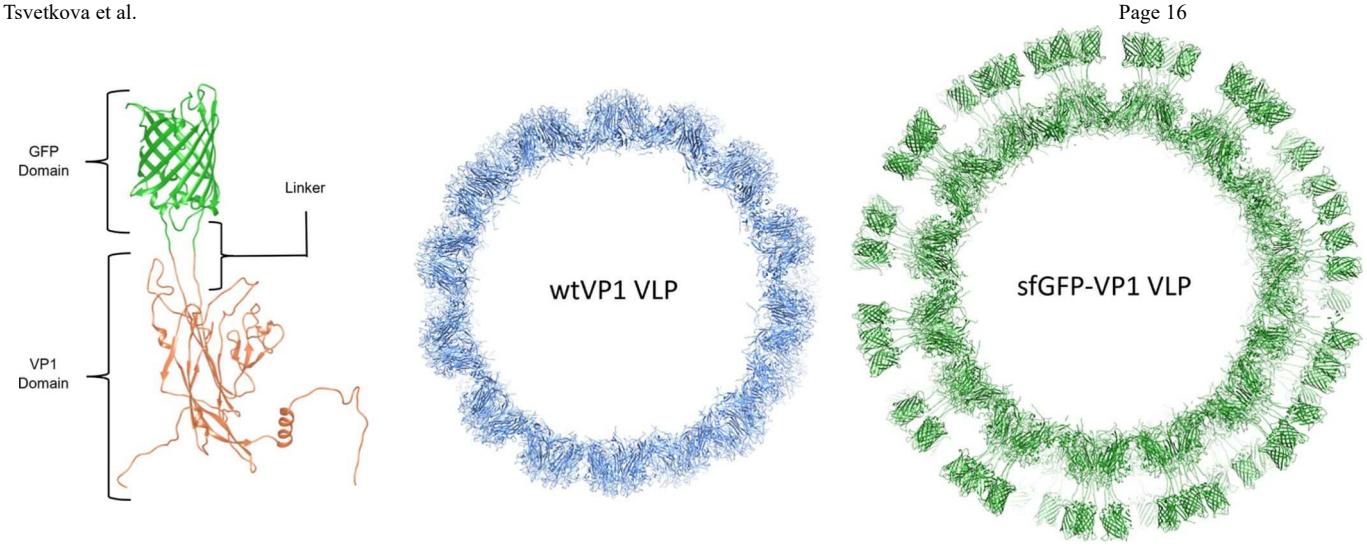

Figure 1.

Molecular models illustrating the sfGFP-VP1 fusion protein, the original T = 7 VP1 cage (~50 nm diameter), and the sfGFP-VP1VLP (~63 nm). Note the crowding of sfGFP in the surface layer, even under a fully extended linker assumption.

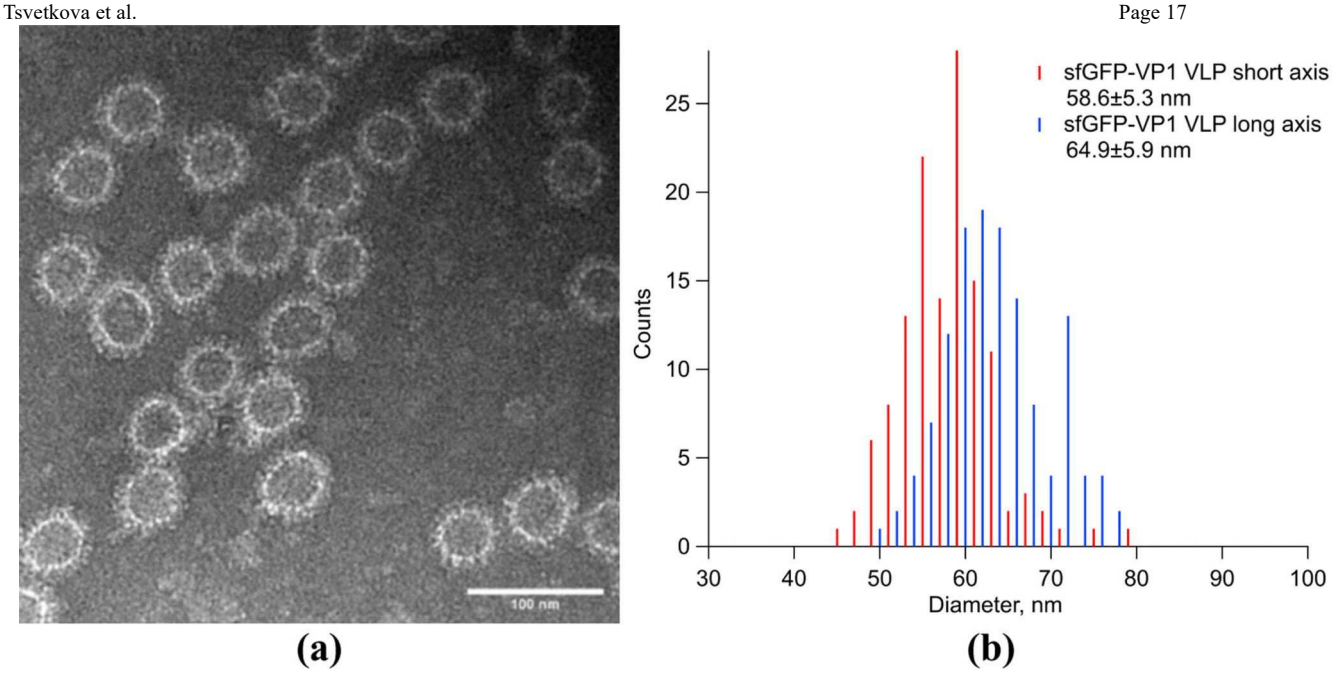

Figure 2.

(a) Negative stain TEM micrograph of sfGFP-VP1VLPs. (b) Histograms of particle diameters measured from negative stain TEM.

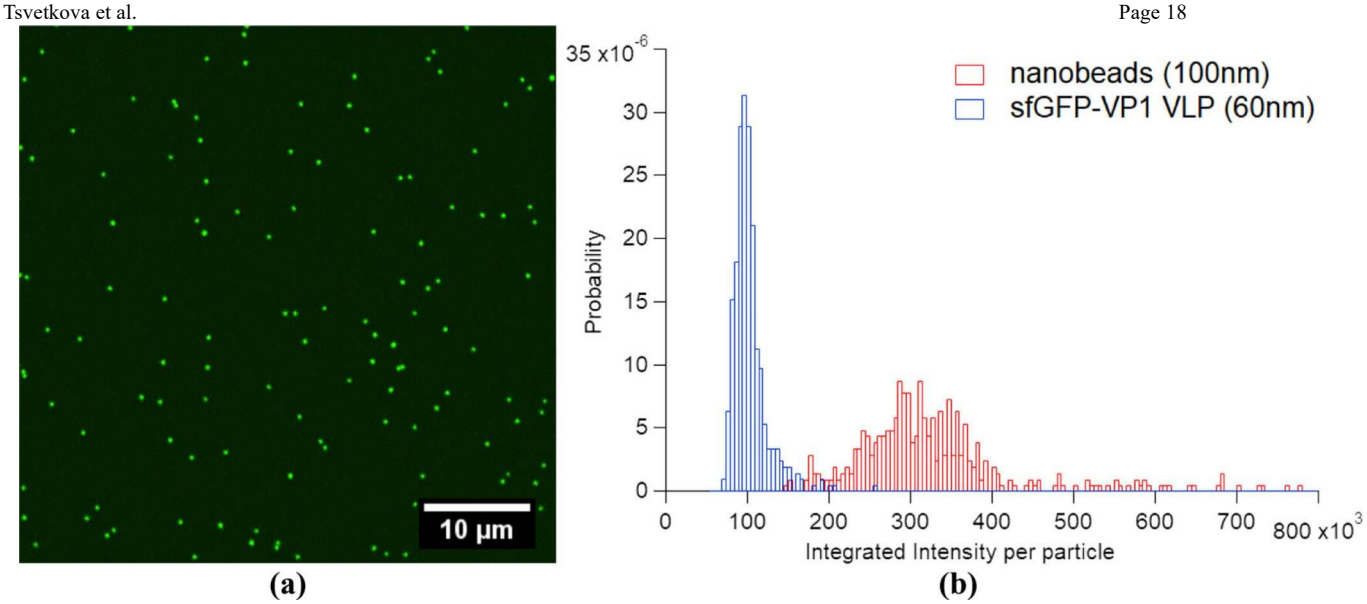

Figure 3.

(a) Spinning disk confocal microscopy of a spread of single sfGFP-VP1VLPs on a glass coverslip, in buffer. (b) Histograms of single-particle, spot-averaged, emission intensities, for sfGFP-VP1VLPs and the nanobeads control under the same illumination/detection parameters.

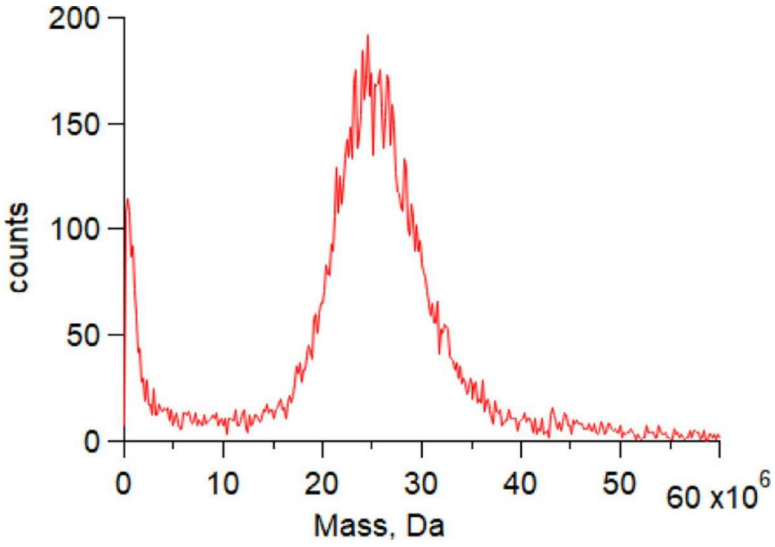

Figure 4.
Mass histogram from CD-MS data collected from fGFP-VP1VLPs.

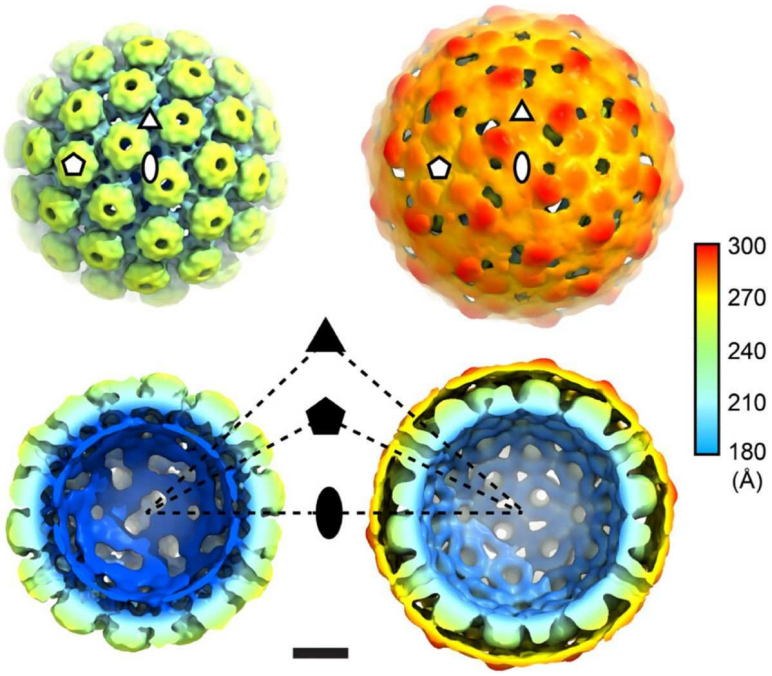

Figure 5.

Cryo-EM structure of yeast derived wtVP1VLPs (left) and sfGFP-VP1VLP (right). Oval, triangle, and pentagon indicate locations of 2-fold, 3-fold and 5-fold axes, respectively. Scale bar is 100 Å.

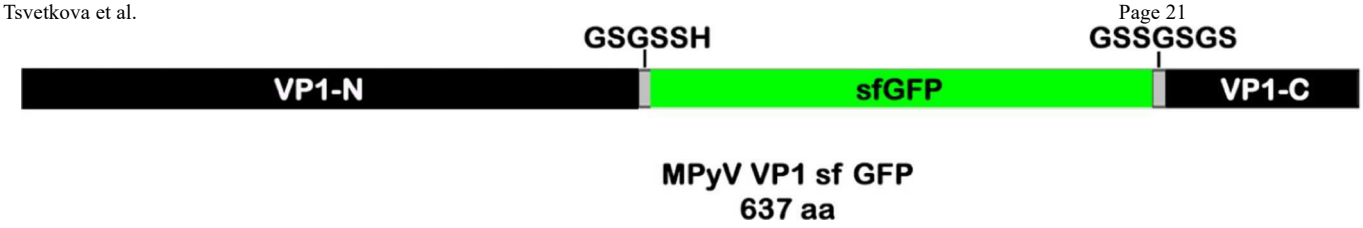

Figure 6.
Plasmid construct.

Table 1.

Statistical Parameters from Measurements of Fluorescence emission from VLPs and 100 nm Nanobeads

	VLP	Nanobead
<p >; (kcts)	99	320
r.m.s.d./< p >; (%)	21%	35%